
Article:
Greig, J. and Bulgakova, N. orcid.org/0000-0002-3780-8164 (2020) Arf6 determines tissue architecture by stabilizing intercellular adhesion. Philosophical Transactions B: Biological Sciences, 375 (1809). 20190682. ISSN 0962-8436

https://doi.org/10.1098/rstb.2019.0682

Arf6 determines tissue architecture by stabilizing intercellular adhesion.

Joshua Greig[1], Natalia A. Bulgakova[1, *]

[1] Department of Biomedical Science and Bateson Centre, The University of Sheffield, Sheffield S10 2TN, United Kingdom.

[*] Corresponding author: n.bulgakova@sheffield.ac.uk

Running title: Arf6 stabilizes intercellular adhesion

Keywords: Arf6**,** cell shape, epithelium, adhesion, actin, endocytosis

Wordcount: 7765

Abstract

Correct cell shape is indispensable for tissue architecture, with cell shape being determined by cortical actin and surface adhesion. The role of adhesion in remodeling tissue is to counteract the deformation of cells by force, resulting from actomyosin contractility, and to maintain tissue integrity. The dynamics of this adhesion is critical to the processes of cell shape formation and maintenance. Here, we show that the trafficking molecule, Arf6, has a direct impact on cell elongation, by acting to stabilize E-cadherin-based adhesion complexes at the cell surface, in addition to its canonical role in endocytosis. We demonstrate that these functions of Arf6 are dependent on the molecule Flotillin1, which recruits Arf6 to the plasma membrane. Our data suggest that Arf6 and Flotillin1 operate in a pathway distinct from clathrin-mediated endocytosis. Altogether, we demonstrate that Arf6- and Flotillin1-dependent regulation of the dynamics of cell adhesion contributes to molding tissue *in vivo*.

Introduction

Tissue architecture is determined by the shapes of the individual cells of which it is composed, with cell shape in the plane of cell-cell adhesion being crucial for the architecture of epithelial monolayers [1]. In these epithelia, cell shape in the apical adhesion plane is the product of cortical actomyosin and intercellular adhesion [2]. This intercellular adhesion is mediated by proteins on the cell surface which bind to molecules on adjacent cells and form stable attachments. The primary adhesion molecule in epithelial cells is E-cadherin (E-cad) which is instrumental in both the formation and maintenance of tissues [3,4]. In morphogenesis, E-cad stabilizes new contacts during cell rearrangements [5] and expands contact length between neighbouring cells [6], regulating final tissue architecture. However, these adhesion sites are not static but highly dynamic, with alterations in this dynamics resulting in abnormal cell shapes and rearrangements [7–10]. Therefore, both the dynamics of adhesion and levels are critical to tissue architecture.

E-cad molecules at the cell surface are constantly removed from the plasma membrane (PM) by the process of endocytosis [9]. These molecules are then either recycled or degraded and replaced by newly synthesized molecules [11,12]. Multiple pathways of endocytosis exist, with the clathrin-mediated pathway being the best characterised [13]. We have recently discovered that clathrin-mediated endocytosis of E-cad from the PM regulates shape of epidermal cells in the late *Drosophila* embryo [7]. At the same time several clathrin-independent pathways have also been identified [14], and clathrin-independent endocytosis has been implicated in Wingless and Notch signalling in *Drosophila* cells [15,16]. What all of the pathways share is the necessity for specific protein mediators to target and traffic surface proteins between the surface and cytoplasm. One of these mediator groups are the evolutionary conserved small GTPase Arf proteins, a family which participates in all major protein trafficking routes known in cells [17,18]. One of its members – Arf6, the sole

member of the class III Arfs [17,19,20] – acts at the PM to sort cargo, particularly adhesion molecules, in mammalian cells [18,21], and assists the internalisation of these cargos including E-cad [22,23].

The dynamics of E-cad at the PM is determined by both endocytosis and the motion of the molecule itself within the lipid bilayer [12,24]. Techniques such as Fluorescence Recovery After Photobleaching (FRAP) have been instrumental in dissecting the mechanisms of E-cad dynamics at junctions [12,25–29]. This has revealed the existence of at least several subpopulations of E-cad at the cell surface, which are distinguished by their dynamic properties and might correspond to E-cad clusters of different sizes and functions [24,29–31]. Protein-membrane domains within the PM serve as one of the general mechanism to promote such protein clustering [32]. These domains have distinct protein and lipid compositions, and their assembly is facilitated by membrane-associated proteins, such as Flotillins [33]. Flotillins are a family of proteins embedded within the PM lipid bilayer, where they form protrusions into the cytoplasm enabling interactions which can modify the structure of the surroundings [33]. Flotillins participate in a range of fundamental cellular processes across species: endocytosis, signal transduction, and cortical actin dynamics [33]. In mammalian cells, Flotillins have been reported to recruit E-cad and stabilize it at the PM [34,35], but also could be potentially involved in E-cad endocytosis and recycling [35,36].

Here, we demonstrate that Arf6 function contributes to normal tissue architecture in an intact tissue *in vivo* using the *Drosophila* embryonic epidermis as a model. Arf6 acts both by regulating the levels of E-cad at the PM and by enabling the formation of stable adhesion. We further show that Arf6 recruitment to the PM is dependent on Flotillin1, and downregulation of Flotillin1 has the same effect on E-cad dynamics and cell shape as that of Arf6. Taken together, our data demonstrate that Arf6 recruitment to the plasma membrane by

Flotillin1 has the effect of stabilizing E-cad intercellular adhesion and thus, regulating junctional stability and tissue architecture.

Results and discussion

To assess the function of Arf6 in general tissue architecture we used the stage 15 *Drosophila* embryonic epidermis, in which cells are highly elongated in the apical plane and rectangular in appearance (Fig. 1A-D). This elongation produces two distinct cell borders: a short border which is orthogonal to the dorsal-ventral axis (DV), and a long border which faces the anterior-posterior axis (AP) of the embryo (Fig. 1A-C). We downregulated Arf6 function with a dominant negative variant ($Arf6^{DN}$) using the *engrailed* promoter driving GAL4 in the posterior halves of each embryonic segment (*en*::Gal4, Fig. 1C-D). We co-expressed $Arf6^{DN}$ with *UAS*::CD8-Cherry to label the cells. The cells expressing this construct were visibly abnormal (Fig. 1D). Using the aspect ratio of the cells as a measure of correct elongation (the ratio between the long and short cell axis, see materials and methods) we found that cells expressing $Arf6^{DN}$ were less elongated than in the control expressing *UAS*::CD8-Cherry alone ($p=0.04$, Fig. 1D-E). A comparable decrease in the aspect ratio was detected in cells upon downregulation of Arf6 levels with RNAi ($p<0.0001$, Fig. 1D-E). To confirm the efficacy of this knock-down we used Arf6 transgenically tagged with GFP (*UAS::*Arf6-GFP, hereafter Arf6-GFP) expressed using the *en*::Gal4 (Fig. 1F). In the presence of the RNAi we observed a reduction in Arf-GFP signal relative to control which co-expressed Arf6-GFP with CD8-cherry ($p=0.002$, Fig. S1A).

To determine where Arf6 acts within the cell to promote cell elongation, we examined its localisation in our system using Arf6-GFP. In the plane of cell-cell adhesion, Arf6-GFP localised predominantly at the PM, overlapping with E-cad (Fig. 1F). In these epidermal cells E-cad-GFP localised in a thin belt of ~1 μm depth at the cell-cell junctions, below the apical

surface in an approximate 1:2 ratio between the AP and DV cell borders (Fig. 1D,H), consistent with previous observations [7,12,37,38]. Here, we used E-cad tagged with GFP and expressed from a ubiquitous *Ubi-p63E* promoter (E-cad-GFP) [39]. Arf6-GFP signal was distributed uniformly around the cell periphery, in contrast to E-cad ($p=0.77$ and $p<0.0001$, respectively, Fig. 1G-H). These observations were consistent with previous reports [40] and suggested that Arf6 acts at intercellular junctions. This result raised two related questions. First, once at the PM, what does Arf6 do to promote cell elongation? Second, what determines the specific enrichment of Arf6 at the PM? We next sought to answer these questions.

Two known functions of Arf6 could explain its role in cell elongation: vesicle trafficking and regulation of the actin cytoskeleton [22]. Indeed, one of the potential Arf6 regulators – the ArfGEF Steppke – is important for cell morphology and tissue architecture in *Drosophila* embryonic epidermis [41]. First, we tested whether the interaction with cortical actomyosin was important for the role of Arf6 in cell elongation. We used a YFP-tagged variant of non-muscle Myosin-II under the *spaghetti-squash* promoter (hereafter, MyoII-YFP) to visualize the actomyosin cortex (Fig. 2A-B). In control cells at this stage of embryonic development, MyoII-YFP was enriched at the AP cell borders, consistent with previous observations [7,12,38]. Expression of $Arf6^{DN}$ led to a significant increase in the levels of MyoII-YFP at both cell borders ($p=0.0001$, $p=0.04$, Fig. 2B), which is consistent with Arf6 preventing the formation of actin stress fibres by downregulating RhoA [41,42]. To explore this further, we decided to measure the activity of RhoA directly. To this end, we used the biosensor of RhoA-activity, the Rho-binding domain of Anillin (RBD-GFP) [43]. This biosensor localised in a similar fashion to MyoII-YFP, with enrichment at the AP cell borders but strong cytoplasmic signal (Fig. S1B-B'). The expression of $Arf6^{DN}$ had no effect on the localisation and levels of RBD-GFP ($p=0.17$, Fig. S1B-B'). This indicates that either

this biosensor is not sensitive enough to reflect the changes in RhoA activity, or that Arf6 influences MyoII independently of RhoA activity in this system. Overall, the impairment of Arf6 function leads to an increase in MyoII-YFP at the cortex, potentially through a RhoA-independent mechanism, the existence of which has been reported [44,45].

MyoII contractility reduces contact length between cells and contributes to cell shape [2]. However, the increase in MyoII at the cortex following Arf6 downregulation was uniform – about 20% at both AP and DV borders (23 ± 7% and 15 ± 9%, respectively). At the same time no change in the apical cell area was observed ($p=0.47$ and $p=0.83$ for Arf6 RNAi and Arf6^{DN}, respectively, Fig. S1C), which would have been expected in the case of a uniform contact length reduction. This suggested that the anisotropic change in the cell shape following Arf6 downregulation, namely the reduction in cell elongation, is likely to be through a different mechanism rather than only cortical actomyosin activity. We next sought to determine the contribution of the trafficking function of Arf6 to the cell shape phenotype.

Our recent studies have demonstrated key roles for membrane trafficking in the regulation of cell shape and specifically in the elongation of cells in the embryonic epidermis [7]. Arf6 regulates vesicle trafficking between the PM and endosomal system [22,46,47]. Indeed, Arf6 is the primary member of the Arf family which is enriched at the PM, making it an obvious candidate to be involved in endocytic trafficking of adhesion proteins. Therefore, we explored the effects of Arf6 downregulation on intercellular adhesion by measuring the distribution and dynamics of E-cad. In cells expressing Arf6^{DN}, E-cad-GFP was elevated at both the AP and DV cell borders in comparison to control ($p=0.02$ and $p=0.007$, Fig. 2D), indicating a uniform effect consistent with the uniform distribution of Arf6. We confirmed the role of Arf6 in E-cad levels at intercellular junctions using an independent approach to inhibit Arf6 function: the expression of an RNAi targeted to Arf6 led to a similar increase in E-cad-GFP at both the AP and DV cell borders ($p=0.0023$, $p=0.031$, Fig. 2C and E).

As we have previously found that both the levels of E-cad and its dynamics contribute to cell shape [7], we decided to explore the effect of the Arf6^{DN} on the dynamics of E-cad at the cell surface using FRAP. In our previous work we showed E-cad-GFP recovered to 70% and 50% of pre-bleach signal for the DV and AP cell borders respectively [12,37]. In cells expressing the Arf6^{DN} we observed an increased recovery of the E-cad-GFP signal at both cell borders (Fig. 2F-G, Supplementary Table 1). Therefore, impairing Arf6 function results in the reduction of the immobile E-cad fraction, suggesting that it is involved in stabilising E-cad within the cell-cell junctions. Overall, these data support a model whereby Arf6 function has a dual effect on cell adhesion: to modulate E-cad levels and facilitate the formation of stable adhesion complexes.

Neither the elevation of E-cad at the PM nor the increase in the mobile fraction could be explained purely by the Arf6 effect on cortical actomyosin. Myosin II promotes E-cad endocytosis in both *Drosophila* and mammalian cells, and its reduction rather than elevation increases E-cad mobility and *vice versa* [7,8,12,48]. The observed elevation of E-cad at the PM by the impairment of Arf6 function was however consistent with defects in E-cad endocytosis and the known Arf6 function in vesicle trafficking. Such elevation is also observed when E-cad endocytosis is perturbed by other means: for example by hyperactivating RhoA signalling or overexpressing p120-catenin (p120ctn), which stabilize E-cad [7,49]. However, if the effect of Arf6 was exclusively through an impairment of endocytosis it would be predicted to produce an increased amount of immobile E-cad, as reported previously when E-cad endocytosis was prevented by inhibiting the function of dynamin [12]. This further suggested that Arf6 has an additional function and contributes to the formation of the stable fraction of E-cad in addition to its known role in endocytosis.

Therefore, we next examined the role of Arf6 in E-cad stability. A key regulator of E-cad stability at the cell surface is the molecule p120-catenin (p120ctn) [7,37,50,51]. The overexpression of p120ctn stabilizes E-cad within junctions in both mammalian and *Drosophila* cells [7,49,52]. If Arf6 were stabilizing E-cad downstream of p120ctn, one might expect its increased localisation to the PM upon p120ctn overexpression. However, we found that the overexpression of p120ctn, which also elevates Myosin-II [7], did not alter the localisation of Arf6 (Fig. 3A-B), from which we concluded that Arf6 is likely to act independently of p120ctn.

We then asked whether Arf6 was involved in clathrin-mediated endocytosis. We used a transgenically tagged variant of the clathrin light chain (*UAS::*CLC-GFP), and analysed the effect of $Arf6^{DN}$ on clathrin dynamics by measuring the exchange of CLC-GFP in the plane of the cell-cell adhesion using FRAP (Fig. 3C-E). This approach has previously been used to identify defects in clathrin-mediated endocytosis in both mammalian and *Drosophila* cells [7,53]. We observed no difference in the CLC-GFP recovery between the control and $Arf6^{DN}$ expressing cells ($p=0.28$, Fig. 3E). Thus, clathrin dynamics was insensitive to the downregulation of Arf6 function, suggesting that Arf6 operates in a clathrin-independent endocytic pathway in this system.

Therefore, we explored Arf6 involvement in clathrin-independent endocytic pathways. As *Drosophila* have no orthologues of the mammalian caveolae, we turned to Flotillins [54,55]. We used an RNAi targeted against the Flotillin1 protein to downregulate its levels. To explore the connection between Flotillin and Arf6, we measured the effect of knocking-down Flotillin1 on Arf6-GFP (Fig. 3F-G) [33,56]. We downregulated Flotillin1 using two independent RNAi lines (results were identical for both). A significant decrease of Arf6-GFP at the PM was detected at both cell borders in cells expressing the Flotillin1 RNAi ($p=0.002$, $p<0.0001$. Fig. 3F-G). This decrease was accompanied by an increase in Arf6-GFP

signal in the cytoplasm, suggesting a defect in Arf6 recruitment rather than total protein levels (p=0.018, Fig. S1D). Therefore, Arf6 is recruited to the PM downstream of Flotillin1, suggesting that Arf6 functions in a Flotillin-mediated pathway.

Therefore, we wondered if Flotillin1 could be upstream of the stabilizing effect that Arf6 had on E-cad, and if the cell shape defect we observed when perturbing Arf6 was due to this pathway. We found that the levels of E-cad-GFP were elevated at both the AP and DV cell borders upon Flotillin1 downregulation with RNAi (p=0.0025, p=0.0005, Fig. 4A-B), similar to what we observed for Arf6 (see Fig. 2C-E). To determine if Flotillin1 was also altering the turnover of cell adhesion we measured the dynamics of E-cad-GFP in cells expressing Flotillin1 RNAi using FRAP (Fig. 4C-D, Supplementary Table 1). In these cells the recovery of E-cad-GFP was elevated at both the AP and DV cell borders, again reminiscent of the effect of $Arf6^{DN}$ (see Fig. 2F-G). Altogether, these results suggested that Arf6 and Flotillin1 act in the same pathway to stabilize E-cad, with Flotillin1 being required for Arf6 localisation to the PM. Indeed, simultaneous downregulation of Flotillin1 by RNAi with the expression of $Arf6^{DN}$ did not increase E-cad levels beyond the increase caused by either of them alone (p=0.96, p=0.97, Fig. 4F), which further confirms that Flotillin1 and Arf6 act in a single pathway. To explore any effect of Flotillin1 on actomyosin, we examined the distribution of MyoII-YFP in cells expressing Flotillin1 RNAi. We found no significant difference between control cells and those expressing Flotillin1 RNAi at both the AP and DV cell borders (p=0.33, p=0.83 respectively Fig. S1E-E'). This finding contrasts with $Arf6^{DN}$ in which an elevation of MyoII-YFP was observed (see Fig 2.A-B), potentially due to the magnitude of the Arf6 reduction in cells expressing Flotillin1 RNAi being insufficient to exert an effect on MyoII. The similarities and differences in the effects of Flotillin1 RNAi and Arf6 impairment additionally suggest that Arf6 regulates E-cad and MyoII through different and independent mechanisms.

Finally, we explored the role of Flotillins in tissue architecture and compared it with that of Arf6 (Fig. 4E,G). Similar to the inhibition of Arf6, Flotillin1 RNAi reduced cell elongation, measured by aspect ratio, by comparison to control cells ($p<0.0001$ and $p=0.0001$ for two RNAi lines, Fig. 4E,G, Supplementary Table 1). As this reduction of cell elongation occurred without any effect on MyoII (see Fig. S1E), we conclude that it is the dynamics of adhesion which is the primary contributory mechanism in this phenotype. Furthermore, when Flotillin1 RNAi was expressed simultaneously with $Arf6^{DN}$ there was no additive phenotype: cell elongation was affected, but it was reduced to the same degree as Flotillin1 RNAi alone ($p<0.0001$ in comparison to control and $p=0.59$ in comparison to Flotillin1 RNAi, Fig.4E,G). Therefore, the stabilization of E-cad by Flotillin-Arf6 is required for correct cell elongation.

We recently found that hyperstabilization of E-cad, by overexpressing p120ctn or inhibiting endocytosis by expressing the dominant-negative variant of dynamin Shibire, has a similar phenotype: reduced cell elongation [7]. The current study alongside our previous work suggests that the correct dynamics of intercellular adhesion is crucial for cell elongation and tissue architecture: if E-cad is too stable or too dynamic cells fail to expand their long borders to a normal extent. This further highlights the fact that all E-cad subcomplexes contribute to cell shape regulation. However, it is tempting to speculate that they do so through different mechanisms: while endocytosis of mobile E-cad enables membrane and thus junctional remodeling required for elongation, immobilization of stable E-cad is rather more likely to stabilize the junctions following remodeling. Therefore, it is the nature of adhesion rather than simply levels, which is crucial for correct tissue architecture.

One interesting question which we were unable to address is what accounts for this dual function of Arf6 and Flotillin: they are involved in both stabilization and the regulation of E-cad levels at the PM, with the latter suggesting an endocytic component. There is evidence that “immobile” E-cad despite not exchanging at the cell junctions on the time-scale

of a typical FRAP experiment is still turned-over on the scale of approximately 2 hours [26]. It is possible that Arf6-Flotllin targets this slow turning over population of E-cad: following E-cad recruitment to Flotillin domains in the PM it is internalized due to unknown cues.

In summary, we have examined the role of stable cell adhesion in tissue architecture using the trafficking protein Arf6. We discovered that Arf6 function contributes to tissue architecture by regulating cell shape. While Arf6 counteracts cortical actomyosin in what appears to be a RhoA-independent manner, this counteraction is not sufficient to explain the Arf6 function in tissue architecture. Rather, this function is due to the dual role of Arf6 on cell adhesion: both stabilizing and modulating the levels of E-cad. We then uncovered the mechanism of this dual role by identifying that Arf6 operates in a clathrin-independent pathway in *Drosophila* and that the Arf6-mediated stabilization of E-cad requires Flotillin1. Finally, we showed that Flotillins support the formation of stable adhesion complexes and that they function upstream of Arf6 by recruiting it to the PM, which enables the formation and regulation of stable cell adhesion and thus correct tissue architecture.

Materials and Methods

Fly stocks and genetics

Flies were raised on standard medium. The GAL4/UAS system [57] was used for all the specific spatial and temporal expression of transgenic and RNAi experiments. The GAL4 expressional driver used for all experiments was *engrailed::GAL4* (*en*::GAL4, Bloomington number 30564). The following fly stocks were used in this study (Bloomington or Kyoto numbers included where applicable): E-cad-GFP (*Ubi::E-cadherin-GFP*) (109007), E-cad-mCherry (59014), *UAS*::CD8-mCherry (27393), *UAS*::CLC-GFP (7109), *UAS*::Arf6-GFP (65867), *UAS*::Arf6-T27N (DN) [58], *UAS*::Arf6 RNAi (27261), Myosin II-YFP (Kyoto Stock Center 115082), Anillin-GFP [59], *UAS*::p120ctn [7], *UAS*::Shibire^{K44A} (*UAS*::Shi-

DN, 5822), and Flotillin RNAi (36649 and 36700; note, the latter stock is currently not available at Bloomington). The p120ctn mutant genotype was ($p120ctn^{308}$/ Δp120) [7].

Embryo collection and fixation

Embryos were collected at 25°C at 3-hour time intervals and allowed to develop at 18°C for 21 hours to reach the desired developmental stage. Then embryos were dechorionated using 50% sodium hypochlorite (bleach, Invitrogen) in water for 4 minutes, and extensively washed with deionized water prior to fixation. Fixation was performed with a 1:1 solution of 4% formaldehyde (Sigma) in PBS (Phosphate Buffered Saline) and heptane (Sigma) for 20 minutes on an orbital shaker at room temperature. Embryos were then devitellinized in 1:1 solution of methanol and heptane for 20 sec with vigorous agitation. Following subsequent methanol washes the fixed embryo specimens were stored at -20°C in methanol until required.

Embryo live imaging

Embryos were collected and dechorionated as described above. Once washed with deionized water embryos were transferred to apple juice agar segments upon microscope slide. Correct genotypes were selected under a fluorescent microscope (Leica) using a needle. Embryos were positioned and orientated in a row consisting of 6-10 embryos per genotype. Following this, embryos were transferred to pre-prepared microscope slides with Scotch tape and embedded in Halocarbon oil 27 (Sigma). Embryos were left to aerate for 10 minutes prior to covering with a cover slip and imaging.

Immunostaining

The only embryos which were immunostained for E-cad, are those expressing Arf6-GFP and CLC-GFP (Fig. 1F, Fig. 2A, and Fig. 3A,C,D). In all other cases, the native fluorescence of GFP and mCherry was imaged. The embryos were washed three times in 1 ml of PBST (PBS with 0.05% Triton) with gentle rocking. Blocking of the embryos prior to staining was done in 300 µl of a 1% NGS (Normal Goat Serum) in PBST for 1 hour at room temperature with gentle rocking. For staining the blocking solution was removed, 300 µl of the primary antibody: 1:100 rat anti-E-cad (DCAD2, DSHB) in fresh blocking solution was added and the embryos were incubated overnight at 4°C with orbital rotation. Then, embryos were washed three times with 1 ml of PBST. A 300 µl 1:300 dilution of the secondary antibody (goat Cy3-conjugated IgG, Invitrogen) was added, and the embryos incubated either overnight at 4°C with orbital rotation or for 2 hours at room temperature. Then embryos were washed three time with PBST, following which they were incubated with 50-70 µl of Vectashield (Vector Laboratories) and allowed to equilibrate for a period of 2 hours before being mounted on microscope slides (Thermo).

Microscopy, data acquisition and FRAP

All experiments were performed using an up-right Olympus FV1000 confocal microscope with a 60x/1.40 NA oil immersion objective. All measurements were made on dorsolateral epidermal cells of embryos, which were near or just after completion of dorsal closure, corresponding to the end of Stage 15 of embryogenesis. An area encompassing two adjacent engrailed domains was imaged to ensure a minimum of 25 cells would be analysed for each embryo. For fixed samples 16-bit images were taken at a magnification of 0.051µm/pixel (1024x1024 pixel XY-image) with a pixel dwell of 4µm/pixel. For each embryo, a Z-axis sectional stack through the plane of the AJs was taken, which consisted of six sections with a

0.38 µm intersectional spacing. The images were saved in the Olympus binary image format for further processing.

For E-cad FRAP (adapted from [12]) 16-bit images were taken at a magnification of 0.093 µm/pixel (320x320 pixel XY-image). In each embryo, several circular regions of 1 µm radius were photobleached at either DV or AP junctions resulting in one bleach event per cell. Photobleaching was performed with 8 scans at 2 µs/pixel at 50-70% 488 nm laser power, resulting in the reduction of E-cad-GFP signal by 60–80%. A stack of 6 z-sections spaced by 0.38 µm was imaged just before photobleaching, and immediately after photobleaching, and then at 20 s intervals, for a total of 15 minutes.

For CLC-GFP FRAP, 16-bit images were taken at a magnification of 0.051µm/pixel (256x256 pixel XY-image). In each embryo a single plane was selected in centre of the cell-cell adhesion band using E-cad-mCherry for positioning. An area encompassing a transverse region orthogonal to the axis of the engrailed expressing cells was selected (140x60 pixels) was photobleached with 1 scan at 2 µm/pixel using 100% 488nm laser power resulting in reduction of CLC-GFP signal by 70-80%. Images were taken using continuous acquisition at a frame rate of 2 sec^{-1}. Prior to bleaching a sequence of 10 images was taken, and a total of 400 frames corresponding to 3.5 minutes were taken.

Data processing and statistical analysis

Membrane intensity and cell shape: Images were processed in Fiji (https://fiji.sc) by generating average intensity projections of the channel required for quantification. Masks were created by processing background-subtracted maximum intensity projections using the Tissue Analyzer plugin in Fiji [60]. Quantification of the membrane intensity at the AP and DV borders and cell elongation (aspect ratio) was done as described previously using a custom-built Matlab script [37] found at (https://github.com/nbul/Intensity). In short, cells

were identified as individual objects using the created masks, and their eccentricities were calculated. The aspect ratio was calculated from the eccentricity as $AR = 1/\sqrt{1 - e^2}$, where *e* is eccentricity. At the same time, the individual borders were identified as objects by subtracting a dilated mask of vertices from a dilated mask of cell outlines. The mean intensity and orientation of each border were calculated. The average border intensities (0-10° for the AP and 40-90° for the DV borders relatively to cell mean orientation) were calculated for each embryo and used as individual data points to compare datasets. The average cytoplasmic intensity was used for the background subtraction. Statistical analysis was performed in Graphpad Prism (https://www.graphpad.com/scientific-software/prism/). First, the data was cleaned using ROUT detection of outliers in Prism followed by testing for normal distribution (D'Agostino & Pearson normality test). Then, the significance for parametric data was tested by either a two-way ANOVA or two-tailed t-test with Welch's correction.

E-cad FRAP: images were processed by using the grouped Z-projector plugin in Fiji to generate average intensity projections for each time-point. Following this the bleached ROI, control ROI and background intensity were manual measured for each time point. This data was processed in Microsoft Excel. First the intensity of the bleached ROI at each time point was background subtracted and normalized as following: $I_n = (F_n - BG_n)/(FC_n - BG_n)$, where F_n – intensity of the bleached ROI at the time point *n*, FC_n – intensity of the control unbleached ROI of the same size at the plasma membrane at the time point *n*, and BG_n – background intensity, measured with the same size ROI in cytoplasm at the time point *n*. Than the relative recovery at each time point was calculated using the following formula: $R_n = (I_n - I_1)/(I_0 - I_1)$, where I_n, I_1 and I_0 are normalized intensities of bleached ROI and time point *n*, immediately after photobleaching, and before photobleaching respectively. These values were input to Prism and nonlinear regression analysis was performed to test for best fit model and if recoveries were significantly different between cell borders or

genotypes. The recovery was fit to either single exponential model in a form of $f(t) = 1 - F_{im} - A_1 e^{-t/T_{fast}}$, or to bi-exponential model in a form of $f(t) = 1 - F_{im} - A_1 e^{-t/T_{fast}} - A_2 e^{-t/T_{slow}}$, where F_{im} is a size of the immobile fraction, T_{fast} and T_{slow} are the half times, and A_1 and A_2 are amplitudes of the fast and slow components of the recovery. An F-test was used to choose the model and compare datasets.

CLC-GFP FRAP: measurements of all intensities, i.e. the bleached ROI, control ROI and the background, and normalization were done using a custom-build Matlab script (http://github.com/nbul/FRAP) using the same algorithm as described for E-cad FRAP. Curve fitting and statistical analysis was performed in Graphpad Prism using a nonlinear regression analysis as described for E-cad FRAP.

Acknowledgments

The authors also wish to acknowledge the help of Professor David Strutt and Dr Kyra Campbell, both of the University of Sheffield. The authors thank the technical staff of the Wolfson Light Microscopy Facility (LMF) and the Fly Facility, the University of Sheffield, without whom this work would not be possible. This work was supported by grant BB/P007503/1 from the UK Biotechnology and Biological Sciences Research Council.

Author Contribution

J.G and N.A.B. designed and performed experiments and wrote the manuscript.

Conflicts of Interest

The authors declare and confirm that there is no conflict of interest for the work presented in this paper.

References

1. Farhadifar R, Röper J-C, Aigouy B, Eaton S, Jülicher F. 2007 The influence of cell mechanics, cell-cell interactions, and proliferation on epithelial packing. *Curr. Biol.* **17**, 2095–2104. (doi:10.1016/j.cub.2007.11.049)

2. Lecuit T, Lenne P-F. 2007 Cell surface mechanics and the control of cell shape, tissue patterns and morphogenesis. *Nat Rev Mol Cell Biol* **8**, 633–644. (doi:10.1038/nrm2222)

3. Harris TJC, Tepass U. 2010 Adherens junctions: from molecules to morphogenesis. *Nat. Rev. Mol. Cell Biol.* **11**, 502–514. (doi:10.1038/nrm2927)

4. Maître J-L, Heisenberg C-P. 2013 Three functions of cadherins in cell adhesion. *Curr. Biol.* **23**, R626-633. (doi:10.1016/j.cub.2013.06.019)

5. Collinet C, Rauzi M, Lenne P-F, Lecuit T. 2015 Local and tissue-scale forces drive oriented junction growth during tissue extension. *Nat. Cell Biol.* **17**, 1247–1258. (doi:10.1038/ncb3226)

6. Vries WN de, Evsikov AV, Haac BE, Fancher KS, Holbrook AE, Kemler R, Solter D, Knowles BB. 2004 Maternal β-catenin and E-cadherin in mouse development. *Development* **131**, 4435–4445. (doi:10.1242/dev.01316)

7. Greig J, Bulgakova NA. 2019 Interplay between cortical actin and E-cadherin dynamics regulates cell shape in the Drosophila embryonic epidermis. *bioRxiv* , 801456. (doi:10.1101/801456)

8. Levayer R, Pelissier-Monier A, Lecuit T. 2011 Spatial regulation of Dia and Myosin-II by RhoGEF2 controls initiation of E-cadherin endocytosis during epithelial morphogenesis. *Nat. Cell Biol.* **13**, 529–540. (doi:10.1038/ncb2224)

9. Brüser L, Bogdan S. 2017 Adherens Junctions on the Move-Membrane Trafficking of E-Cadherin. *Cold Spring Harb Perspect Biol* **9**. (doi:10.1101/cshperspect.a029140)

10. West JJ, Harris TJC. 2016 Cadherin Trafficking for Tissue Morphogenesis: Control and Consequences. *Traffic* **17**, 1233–1243. (doi:10.1111/tra.12407)

11. Le TL, Yap AS, Stow JL. 1999 Recycling of E-Cadherin: A Potential Mechanism for Regulating Cadherin Dynamics. *The Journal of Cell Biology* **146**, 219–232. (doi:10.1083/jcb.146.1.219)

12. Bulgakova NA, Grigoriev I, Yap AS, Akhmanova A, Brown NH. 2013 Dynamic microtubules produce an asymmetric E-cadherin–Bazooka complex to maintain segment boundaries. *J Cell Biol* **201**, 887–901. (doi:10.1083/jcb.201211159)

13. Aguilar RC, Wendland B. 2005 Endocytosis of membrane receptors: two pathways are better than one. *Proc. Natl. Acad. Sci. U.S.A.* **102**, 2679–2680. (doi:10.1073/pnas.0500213102)

14. Hemalatha A, Mayor S. 2019 Recent advances in clathrin-independent endocytosis. *F1000Res* **8**. (doi:10.12688/f1000research.16549.1)

15. Hemalatha A, Prabhakara C, Mayor S. 2016 Endocytosis of Wingless via a dynamin-independent pathway is necessary for signaling in Drosophila wing discs. *PNAS* **113**, E6993–E7002. (doi:10.1073/pnas.1610565113)

16. Shimizu H, Woodcock SA, Wilkin MB, Trubenová B, Monk NAM, Baron M. 2014 Compensatory Flux Changes within an Endocytic Trafficking Network Maintain Thermal Robustness of Notch Signaling. *Cell* **157**, 1160–1174. (doi:10.1016/j.cell.2014.03.050)

17. D'Souza-Schorey C, Chavrier P. 2006 ARF proteins: roles in membrane traffic and beyond. *Nature Reviews Molecular Cell Biology* **7**, nrm1910. (doi:10.1038/nrm1910)

18. Palacios F. 2001 An essential role for ARF6-regulated membrane traffic in adherens junction turnover and epithelial cell migration. *The EMBO Journal* **20**, 4973–4986. (doi:10.1093/emboj/20.17.4973)

19. Donaldson JG, Jackson CL. 2011 ARF family G proteins and their regulators: roles in membrane transport, development and disease. *Nature Reviews Molecular Cell Biology* **12**, 362–375. (doi:10.1038/nrm3117)

20. Jackson CL, Bouvet S. 2014 Arfs at a Glance. *Journal of Cell Science* **127**, 4103–4109. (doi:10.1242/jcs.144899)

21. Sabe H. 2003 Requirement for Arf6 in cell adhesion, migration, and cancer cell invasion. *J. Biochem.* **134**, 485–489. (doi:10.1093/jb/mvg181)

22. Donaldson JG. 2003 Multiple Roles for Arf6: Sorting, Structuring, and Signaling at the Plasma Membrane. *J. Biol. Chem.* **278**, 41573–41576. (doi:10.1074/jbc.R300026200)

23. Schweitzer JK, Sedgwick AE, D'Souza-Schorey C. 2011 ARF6-mediated endocytic recycling impacts cell movement, cell division and lipid homeostasis. *Semin Cell Dev Biol* **22**, 39–47. (doi:10.1016/j.semcdb.2010.09.002)

24. Erami Z, Timpson P, Yao W, Zaidel-Bar R, Anderson KI. 2015 There are four dynamically and functionally distinct populations of E-cadherin in cell junctions. *Biology Open* , bio.014159. (doi:10.1242/bio.014159)

25. Etournay R *et al.* 2015 Interplay of cell dynamics and epithelial tension during morphogenesis of the Drosophila pupal wing. *Elife* **4**, e07090. (doi:10.7554/eLife.07090)

26. Iyer KV, Piscitello-Gómez R, Jülicher F, Eaton S. 2018 Mechanosensitive binding of p120-Catenin at cell junctions regulates E-Cadherin turnover and epithelial viscoelasticity. *bioRxiv* , 357186. (doi:10.1101/357186)

27. Erami Z *et al.* 2015 Intravital FRAP Imaging using an E-cadherin-GFP Mouse Reveals Disease- and Drug-Dependent Dynamic Regulation of Cell-Cell Junctions in Live Tissue. *Cell Rep* **14**, 152–167. (doi:10.1016/j.celrep.2015.12.020)

28. Huang J, Huang L, Chen Y-J, Austin E, Devor CE, Roegiers F, Hong Y. 2011 Differential regulation of adherens junction dynamics during apical–basal polarization. *J Cell Sci* **124**, 4001–4013. (doi:10.1242/jcs.086694)

29. Cavey M, Rauzi M, Lenne P-F, Lecuit T. 2008 A two-tiered mechanism for stabilization and immobilization of E-cadherin. *Nature* **453**, 751–756. (doi:10.1038/nature06953)

30. Strale P-O *et al.* 2015 The formation of ordered nanoclusters controls cadherin anchoring to actin and cell–cell contact fluidity. *J Cell Biol* **210**, 333–346. (doi:10.1083/jcb.201410111)

31. Indra I, Choi J, Chen C-S, Troyanovsky RB, Shapiro L, Honig B, Troyanovsky SM. 2018 Spatial and temporal organization of cadherin in punctate adherens junctions. *PNAS* , 201720826. (doi:10.1073/pnas.1720826115)

32. Truong-Quang B-A, Lenne P-F. 2014 Membrane microdomains: from seeing to understanding. *Front Plant Sci* **5**. (doi:10.3389/fpls.2014.00018)

33. Otto GP, Nichols BJ. 2011 The roles of flotillin microdomains – endocytosis and beyond. *J Cell Sci* **124**, 3933–3940. (doi:10.1242/jcs.092015)

34. Chartier NT, Lainé MG, Ducarouge B, Oddou C, Bonaz B, Albiges-Rizo C, Jacquier-Sarlin MR. 2011 Enterocytic differentiation is modulated by lipid rafts-dependent assembly of adherens junctions. *Exp. Cell Res.* **317**, 1422–1436. (doi:10.1016/j.yexcr.2011.03.009)

35. Guillaume E, Comunale F, Do Khoa N, Planchon D, Bodin S, Gauthier-Rouvière C. 2013 Flotillin microdomains stabilize cadherins at cell-cell junctions. *J. Cell. Sci.* **126**, 5293–5304. (doi:10.1242/jcs.133975)

36. Solis GP, Hülsbusch N, Radon Y, Katanaev VL, Plattner H, Stuermer CAO. 2013 Reggies/flotillins interact with Rab11a and SNX4 at the tubulovesicular recycling compartment and function in transferrin receptor and E-cadherin trafficking. *MBoC* **24**, 2689–2702. (doi:10.1091/mbc.e12-12-0854)

37. Bulgakova NA, Brown NH. 2016 Drosophila p120-catenin is crucial for endocytosis of the dynamic E-cadherin-Bazooka complex. *J. Cell. Sci.* **129**, 477–482. (doi:10.1242/jcs.177527)

38. de Matos Simões S, Blankenship JT, Weitz O, Farrell DL, Tamada M, Fernandez-Gonzalez R, Zallen JA. 2010 Rho-kinase directs Bazooka/Par-3 planar polarity during Drosophila axis elongation. *Dev Cell* **19**, 377–388. (doi:10.1016/j.devcel.2010.08.011)

39. Oda H, Tsukita S. 2001 Real-time imaging of cell-cell adherens junctions reveals that Drosophila mesoderm invagination begins with two phases of apical constriction of cells. *J. Cell. Sci.* **114**, 493–501.

40. Lee DM, Rodrigues FF, Yu CG, Swan M, Harris TJC. 2015 PH Domain-Arf G Protein Interactions Localize the Arf-GEF Steppke for Cleavage Furrow Regulation in Drosophila. *PLOS ONE* **10**, e0142562. (doi:10.1371/journal.pone.0142562)

41. West JJ, Zulueta-Coarasa T, Maier JA, Lee DM, Bruce AEE, Fernandez-Gonzalez R, Harris TJC. 2017 An Actomyosin-Arf-GEF Negative Feedback Loop for Tissue Elongation under Stress. *Current Biology* **27**, 2260-2270.e5. (doi:10.1016/j.cub.2017.06.038)

42. Boshans RL, Szanto S, van Aelst L, D'Souza-Schorey C. 2000 ADP-Ribosylation Factor 6 Regulates Actin Cytoskeleton Remodeling in Coordination with Rac1 and RhoA. *Mol Cell Biol* **20**, 3685–3694.

43. Mason FM, Xie S, Vasquez CG, Tworoger M, Martin AC. 2016 RhoA GTPase inhibition organizes contraction during epithelial morphogenesis. *J Cell Biol* **214**, 603–617. (doi:10.1083/jcb.201603077)

44. Uehara R, Goshima G, Mabuchi I, Vale RD, Spudich JA, Griffis ER. 2010 Determinants of Myosin II Cortical Localization during Cytokinesis. *Curr Biol* **20**, 1080–1085. (doi:10.1016/j.cub.2010.04.058)

45. Borges RM, Lamers ML, Forti FL, Santos MFD, Yan CYI. 2011 Rho signaling pathway and apical constriction in the early lens placode. *Genesis* **49**, 368–379. (doi:10.1002/dvg.20723)

46. D'Souza-Schorey C, van Donselaar E, Hsu VW, Yang C, Stahl PD, Peters PJ. 1998 ARF6 Targets Recycling Vesicles to the Plasma Membrane: Insights from an Ultrastructural Investigation. *J Cell Biol* **140**, 603–616.

47. Van Acker T, Tavernier J, Peelman F. 2019 The Small GTPase Arf6: An Overview of Its Mechanisms of Action and of Its Role in Host–Pathogen Interactions and Innate Immunity. *Int J Mol Sci* **20**. (doi:10.3390/ijms20092209)

48. Ratheesh A *et al.* 2012 Centralspindlin and α-catenin regulate Rho signalling at the epithelial zonula adherens. *Nat Cell Biol* **14**, 818–828. (doi:10.1038/ncb2532)

49. Hunter MV, Lee DM, Harris TJC, Fernandez-Gonzalez R. 2015 Polarized E-cadherin endocytosis directs actomyosin remodeling during embryonic wound repair. *J Cell Biol* **210**, 801–816. (doi:10.1083/jcb.201501076)

50. Reynolds AB. 2007 p120-catenin: Past and present. *Biochimica et Biophysica Acta (BBA) - Molecular Cell Research* **1773**, 2–7. (doi:10.1016/j.bbamcr.2006.09.019)

51. Ireton RC *et al.* 2002 A novel role for p120 catenin in E-cadherin function. *J Cell Biol* **159**, 465–476. (doi:10.1083/jcb.200205115)

52. Cadwell CM, Su W, Kowalczyk AP. 2016 Cadherin Tales: Regulation of Cadherin Function by Endocytic Membrane Trafficking. *Traffic* (doi:10.1111/tra.12448)

53. Wu X, Zhao X, Baylor L, Kaushal S, Eisenberg E, Greene LE. 2001 Clathrin exchange during clathrin-mediated endocytosis. *J Cell Biol* **155**, 291–300. (doi:10.1083/jcb.200104085)

54. Bodin S, Planchon D, Rios Morris E, Comunale F, Gauthier-Rouvière C. 2014 Flotillins in intercellular adhesion - from cellular physiology to human diseases. *J. Cell. Sci.* **127**, 5139–5147. (doi:10.1242/jcs.159764)

55. Katanaev VL, Solis GP, Hausmann G, Buestorf S, Katanayeva N, Schrock Y, Stuermer CAO, Basler K. 2008 Reggie-1/flotillin-2 promotes secretion of the long-range signalling forms of Wingless and Hedgehog in Drosophila. *EMBO J.* **27**, 509–521. (doi:10.1038/sj.emboj.7601981)

56. Babuke T, Ruonala M, Meister M, Amaddii M, Genzler C, Esposito A, Tikkanen R. 2009 Hetero-oligomerization of reggie-1/flotillin-2 and reggie-2/flotillin-1 is required for their endocytosis. *Cell. Signal.* **21**, 1287–1297. (doi:10.1016/j.cellsig.2009.03.012)

57. Brand AH, Perrimon N. 1993 Targeted gene expression as a means of altering cell fates and generating dominant phenotypes. *Development* **118**, 401–415.

58. Chen EH, Pryce BA, Tzeng JA, Gonzalez GA, Olson EN. 2003 Control of myoblast fusion by a guanine nucleotide exchange factor, loner, and its effector ARF6. *Cell* **114**, 751–762.

59. Munjal A, Philippe J-M, Munro E, Lecuit T. 2015 A self-organized biomechanical network drives shape changes during tissue morphogenesis. *Nature* **524**, 351–355. (doi:10.1038/nature14603)

60. Aigouy B, Umetsu D, Eaton S. 2016 Segmentation and Quantitative Analysis of Epithelial Tissues. *Methods Mol. Biol.* **1478**, 227–239. (doi:10.1007/978-1-4939-6371-3_13)

Figure 1. Arf6 function contributes to correct cell shape and is localised to the Adherens junction.

(**A-C**) Overview of the stage 15 *Drosophila* embryonic epidermis. (**A**) Cartoon sketch of the embryo; area indicated by red box is the dorsolateral epidermis imaged in this study. (**B**) Schematic of the cell morphology in the tissue and the two cell borders present in these cells: the long anterior-posterior (AP, red) and short dorsal-ventral (DV, blue). (**C**) Apical view of the epidermis highlighted in the red box (**A**). Cells are outlined by E-cad-GFP (green) and the *engrailed* compartments which express all transgenic construct used in this study are highlighted by CD8-mCherry (magenta). (**D-E**) Examples (**D**) and aspect ratio (**E**) of cells expressing CD8-mCherry alone (control; magenta, in **C**), and co-expressing it with the $Arf6^{DN}$ (magenta, middle in **D**) and Arf6-RNAi (magenta, bottom in **D**). E-cad-GFP marks cell morphology (green, left; grey, right images in **D**). The area of images in **D** is indicated by the box in (**C**). **(F-G).** Localisation of the Arf6-GFP in the apical region of the epidermal cells corresponding with the plane of cell-cell adherens junction with a representative image (**F**) and quantification (**G**). Arf6-GFP was expressed in the *engrailed* (green, left; and grey, right in **F**). (**H**) Levels of E-cad- GFP at the two cells borders of the epidermal cells. Statistical analysis is a two-tailed students t-test with Welch's correction. Scale bars – 10 μm *, $p < 0.05$; ****, $p < 0.0001$. Each dot represents an individual embryo, n number was 10-20 embryos per genotype with a minimum of 28 cells imaged per embryo.

Figure 2. Arf6 function alters both Myosin-II localisation and the levels and dynamics of E-cad.

(**A-B**) Representative images (**A**) and levels (**B**) of MyoII-YFP (Right in A) in the epidermis of internal control and $Arf6^{DN}$ expressing embryos. Cell borders were visualized with antibody against E-cad (green in **A**) and cells expressing $Arf6^{DN}$ transgene marked by CD8-

mCherry (magenta). (**C-G**) Levels (**C-E**) and dynamics (**F-G**) of E-cad in Arf6 knock-down or dominant negative. **(C-E**) Representative images (**C**) and levels (**D-E**) of E-cad in cells expressing CD8-mCherry alone (Control, top), $Arf6^{DN}$ (middle), or an RNAi against Arf6 (bottom). (**F-G**) Representative examples (**F**) and quantification (**G**) of E-cad-GFP FRAP in control and $Arf6^{DN}$ expressing cells. Panels in **F** show the region bleached (Position P, red circle) at the prebleach (Time T-1), bleach (Time T0), and the end (Time T900) time points. Time is in seconds. Average recovery curves (mean ± s.e.m.) and the best-fit curves (solid lines) are shown in **G**. All best-fit and membrane intensity data are in Table S1. Scale bars – 10 μm. Statistical analysis of the two cell borders between the genotypes was performed using a two-way ANOVA. Individual p-values are shown for each border between the genotypes are shown above. *, $p < 0.05$; **, $p < 0.01$; ***, $p < 0.001$, ****, $p < 0.0001$. Each dot represents an individual embryo, n number was 10-20 embryos per genotype with a minimum of 29 cells imaged per embryo. For FRAP 8-10 embryos were used, with two AP and DV cell borders measured per embryo and averaged to give the final embryo value.

Figure 3. Arf6 is separate from clathrin and p120ctn but requires Flotillin1 for recruitment to the cell surface.

(**A-B**). Representative images (**A**) and levels (**B**) of Arf6-GFP (grey, right; green, left in **A**) in control (top in **A**) and the overexpression of p120ctn (bottom in **A**). (**C-E**). Localisation (**C**) and FRAP (**D-E**) of CLC-GFP (grey, **D** and right in **C**; magenta, left in **C**) in the plane of cell-cell adhesion, expressed in the *engrailed* compartment in control cells (top in **C** and **D**) and $Arf6^{DN}$ expressing cells (bottom in **C** and **D**). Panels in **D** show the region bleached (Position P, red square) at the prebleach (Time T-1), bleach (Time T0), and the end (Time T400) time point in seconds. Average recovery curves (mean ± s.e.m.) and the best-fit curves (solid lines) are shown in **E**. All best-fit and membrane intensity data are in Table S1. (**F-G**)

Representative images (**F**) and levels (**G**) of Arf6-GFP (grey, right; green, left in **F**) in control (top in **F**) and Flotillin RNAi expressing cells (bottom in **F**). Scale bars – 10 μm. Cell borders were visualized with antibody against E-cad (magenta, left in **A**, **C**, and **F**). Statistical analysis was performed using a two-way ANOVA. p-values are shown for each border type between the genotypes. **, $p < 0.01$; ****, $p < 0.0001$. Each dot represents an individual embryo, n number was 10-20 embryos per genotype with a minimum of 35 cells imaged per embryo. For FRAP 8-10 embryos were used, with a single rectangular band encompassing an engrailed stripe used per embryo.

Figure 4. Flotillin determines cell shape and E-cad dynamics upstream of Arf6.

(**A-B**). Representative images (**A**) and levels (**B**) of E-cad-GFP (green, left; and grey, right in A) in control (top in A) and Flotillin1 RNAi expressing cells (bottom in A). (C-D) Representative examples (**C**) and quantification (**D**) of E-cad-GFP FRAP in control and Flotillin1 RNAi expressing cells. Panels in **C** show the region bleached (Position P, red circle) at the prebleach (Time T-1), bleach (Time T0), and the end (Time T900) time points. Time is in seconds. Average recovery curves (mean ± s.e.m.) and the best-fit curves (solid lines) are shown in **D**. (**E-F**) Representative images (**E**) and levels (**F**) of E-cad-GFP (green, left: grey, right in **E**) in cells expressing either: Flotillin1 RNAi alone (top in **E**), $Arf6^{DN}$ alone (middle in **E**), or both Flotillin1 RNAi and $Arf6^{DN}$ (bottom in **E**). (**F**) E-cad-GFP levels at cell borders in cells expressing: $Arf6^{DN}$ alone (blue), Flotillin1 RNAi alone (purple), or both: $Arf6^{DN}$ and Flotillin1 RNAi (black). (**G**) Aspect ratio of the cells expressing Flotillin1 RNAi alone, $Arf6^{DN}$ alone, or both Flotillin1 RNAi and $Arf6^{DN}$. Scale bars – 10 μm. RNAi expressing cells marked by CD8-mCherry (magenta, left in **A** and **E**). Statistical analysis was performed using a two-way ANOVA. p-values are shown for each border type between the genotypes. For analysis of aspect ratios, a one-way ANOVA with Turkeys multiple

comparison test was used. *, $p < 0.05$; **, $p < 0.01$; ***, $p < 0.001$. ****, $p < 0.0001$. Each dot represents an individual embryo, n number was 10-20 embryos per genotype with a minimum of 29 cells imaged per embryo. For FRAP 8-10 embryos were used, with two AP and DV cell borders measured per embryo and averaged to give the final embryo value.

Supplementary information

Table S1. Numerical values for each experiment presented in paper.

Figure S1. Control measures of Arf6 RNAi efficacy and the Arf6-Flotillin pathway is independent of RhoA and actomyosin.

(**A**) Quantification of the efficacy of Arf6 RNAi on Arf6-GFP intensity in the epidermal cells. (**B**) Representative images of RBD-GFP localisation in the epidermal cells of control and $Arf6^{DN}$ expressing embryos. Cell borders were visualized with antibody against E-cad (green in **B**) and cells expressing transgene marked by CD8-mCherry (magenta). (**B'**) Quantification of the levels of RBD-GFP at the AP and DV cell borders between control and $Arf6^{DN}$ expressing cells. (**C**) Apical cell area of the cells expressing CD8-mCherry alone (red, Control), $Arf6^{DN}$ (blue), or Arf6 RNAi alone (purple). (**D**) Quantification of the cytoplasmic intensity of Arf6-GFP between control and Flotillin1 expressing cells. (**E**) Representative images of MyoII-YFP localisation in the epidermal cells of control and flotillin1 RNAi expressing embryos. (**E'**) Quantification of MyoII-YFP at both the AP and DV cell borders between the control and Flotillin1 RNAi expressing cells. For A and C, statistical analysis is a two-tailed students t-test with Welch's correction. Scale bars – 10 μm *, $p < 0.05$; **, $p < 0.001$. For B and D, statistical analysis of the two cell borders between the genotypes was performed using a two-way ANOVA. Individual p-values are shown for each border between the genotypes are shown above. Each dot represents an individual

embryo, n number was 10-20 embryos per genotype with a minimum of 24 cells imaged per embryo.

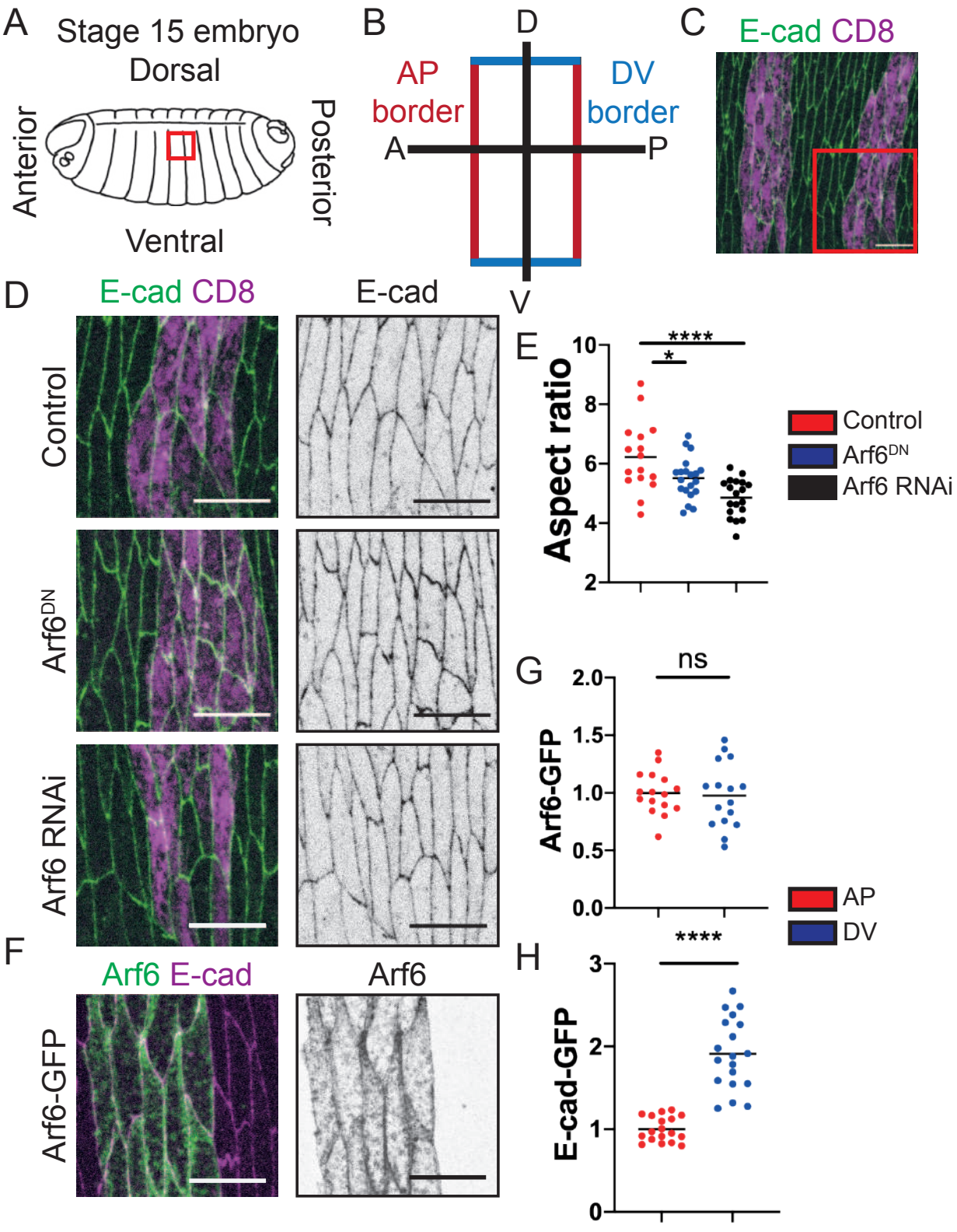
A
Stage 15 embryo
Dorsal
Anterior
Posterior
Ventral
B
D
AP
border
DV
border
A
P
V
C
E-cad CD8
D
E-cad CD8
E-cad
Control
Arf6DN
Arf6 RNAi
E
Aspect ratio
10
8
6
4
2
****
*
Control
Arf6DN
Arf6 RNAi
G
Arf6-GFP
2.0
1.5
1.0
0.5
0.0
ns
AP
DV
F
Arf6 E-cad
Arf6
Arf6-GFP
H
E-cad-GFP
3
2
1
0
****

Fig. 1

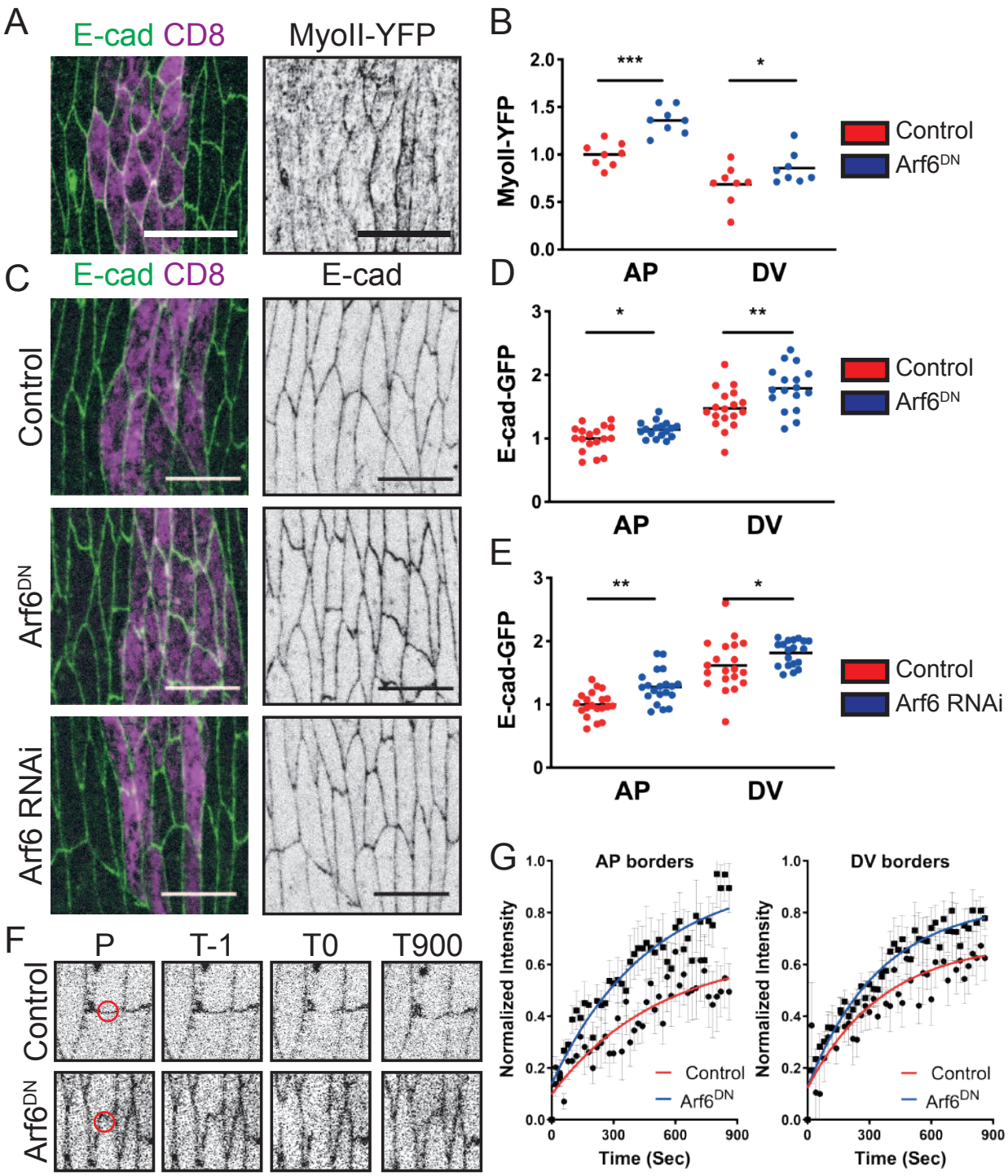
A
E-cad CD8
MyoII-YFP
B
MyoII-YFP
2.0
1.5
1.0
0.5
0.0
***
*
AP
DV
Control
Arf6DN
C
E-cad CD8
E-cad
Control
Arf6DN
Arf6 RNAi
D
E-cad-GFP
3
2
1
0
*
**
AP
DV
Control
Arf6DN
E
E-cad-GFP
**
*
AP
DV
Control
Arf6 RNAi
F
P
T-1
T0
T900
Control
Arf6DN
G
AP borders
DV borders
Normalized Intensity
1.0
0.8
0.6
0.4
0.2
0.0
0
300
600
900
Time (Sec)
Control
Arf6DN

Fig. 2

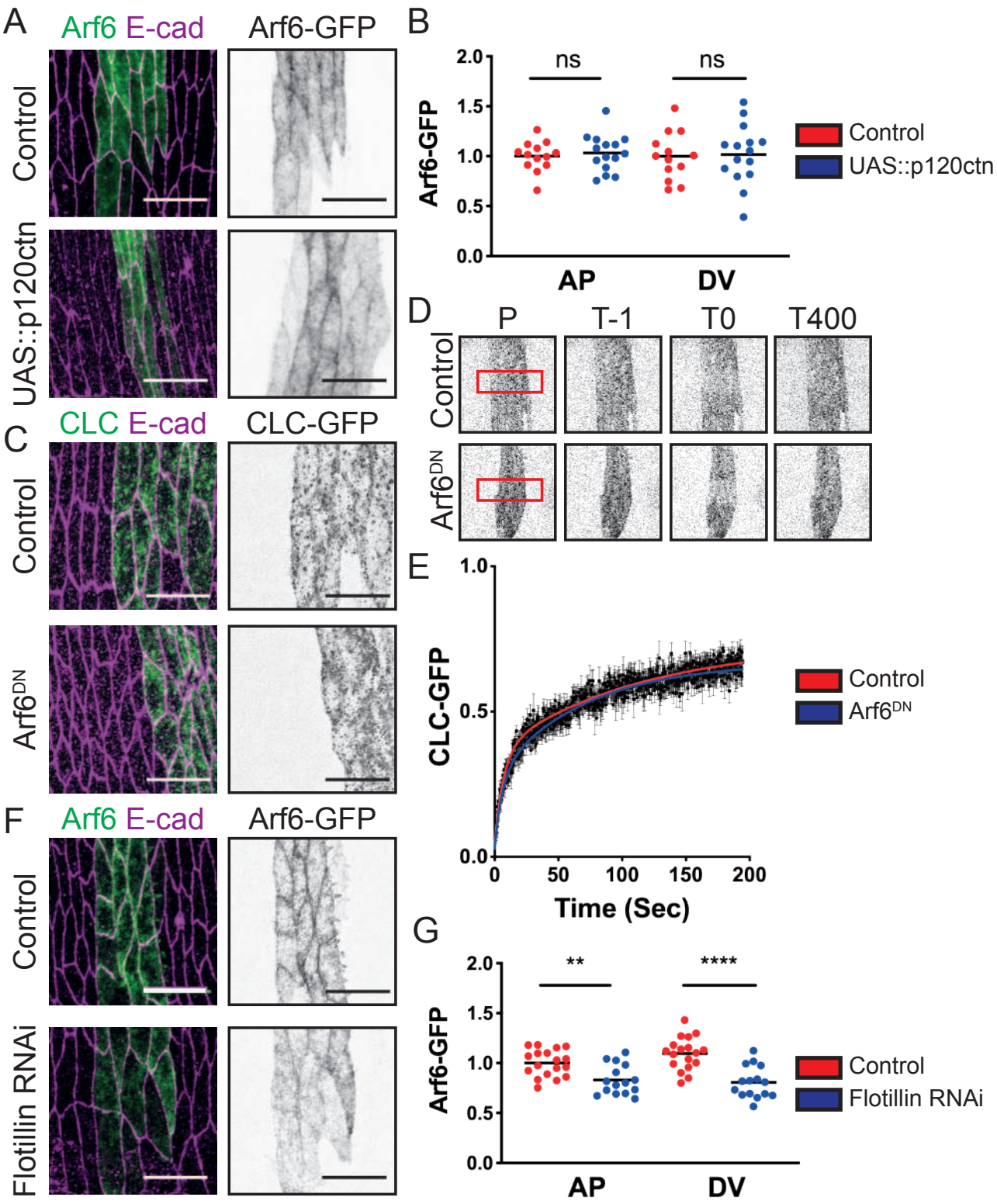
A
Arf6 E-cad
Arf6-GFP
Control
UAS::p120ctn
B
Arf6-GFP
ns
ns
AP
DV
Control
UAS::p120ctn
C
CLC E-cad
CLC-GFP
Control
Arf6DN
D
P
T-1
T0
T400
Control
Arf6DN
E
CLC-GFP
Time (Sec)
Control
Arf6DN
F
Arf6 E-cad
Arf6-GFP
Control
Flotillin RNAi
G
Arf6-GFP
**
****
AP
DV
Control
Flotillin RNAi

Fig. 3

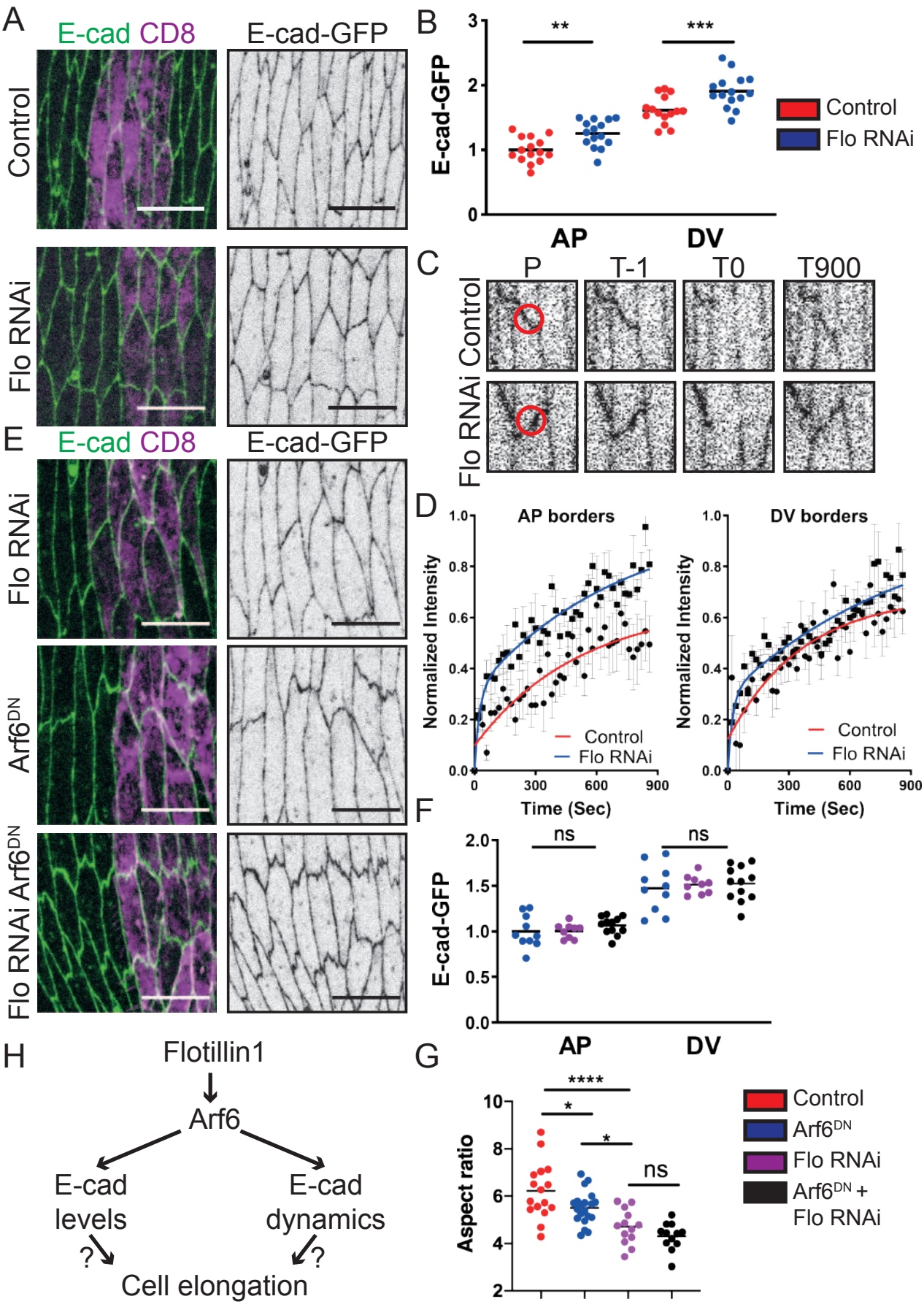
A
E-cad CD8
E-cad-GFP
Control
Flo RNAi
E
Flo RNAi
Arf6DN
Flo RNAi Arf6DN
B
E-cad-GFP
**
***
AP
DV
Control
Flo RNAi
C
P
T-1
T0
T900
Control
Flo RNAi
D
AP borders
DV borders
Normalized Intensity
Time (Sec)
Control
Flo RNAi
F
E-cad-GFP
ns
AP
DV
G
Aspect ratio
****
*
ns
Control
Arf6DN
Flo RNAi
Arf6DN + Flo RNAi
H
Flotillin1
Arf6
E-cad levels
E-cad dynamics
?
Cell elongation

Fig. 4